Separation and Purification Technology 302 (2022) 122087

Contents lists available at ScienceDirect

Separation and Purification Technology

journal homepage: www.elsevier.com/locate/seppur

# Facile construction of Z-scheme AgBr/BiO(HCOO)$_{0.75}$I$_{0.25}$ photocatalyst for visible-light-driven BPA degradation: Catalytic kinetics, selectivity and mechanism

Qiao Wang [a], Yiting Cao [a], Meirui Yu [a], Guanheng Lv [a], Chuyi Zhang [a], Wei Wang [b,*], Jialin Jia [b,*], Zhihong Wang [a]

[a] School of Civil and Transportation Engineering, Guangdong University of Technology, Guangzhou 510006, China
[b] State Key Laboratory of Urban Water Resource and Environment, Harbin Institute of Technology, Harbin 150090, China

ARTICLE INFO

*Keywords:*
Bi-based heterojunction
Z-scheme
Photocatalytic degradation
Selective oxidation

ABSTRACT

Herein, a novel AgBr/BiO(HCOO)$_{0.75}$I$_{0.25}$ Z-scheme photocatalyst was constructed through a facile hydrothermal and post-precipitation method for visible-light (VL) driven wastewater remediation. The 10 wt% AgBr/BiO(HCOO)$_{0.75}$I$_{0.25}$ composite (10%ABB) could completely decompose bisphenol A (BPA) within 25 min, and multiple coexisting inorganic anions and natural organic matters only slightly affected the BPA removal efficiency. The wonderful photocatalytic performance could attribute to the construction of Z-scheme heterojunction, which modulated the energy band, accelerated the electron transfer and also raised the redox ability of the system. Since the superoxide radicals ($O_2^{\bullet-}$) and non-radical pathway ($^1O_2$ and $h^+$) were proved to be the dominating reactive species, 10%ABB/VL system exhibited a highly selective oxidation on aromatics with electron donating groups, whereas a relatively low value for organics with electron with drawing groups. By investigating the ionization potential (IP) of five representative organics, a negative correlation between IP value and reaction kinetics was reported. Moreover, the possible photocatalytic mechanism and elimination pathway were proposed via a series of photoelectrochemical analysis and LC-MS/MS. This work provides a strategy for engineering novel Bi-based photocatalyst and establishing selective oxidation system for organic contamination removal.

## 1. Introduction

As one of the most common endocrine disruptors, bisphenol A (BPA) has been widely applied in the manufacture of epoxy resins, polycarbonate plastics and phenolic resin [1–3]. These chemicals are the raw materials of can linings, water pipes, baby feeding bottles, plastic food packaging products and some paper products [4]. With the global consumption of BPA increasing, BPA was also released into the environment in large quantities [5]. It has been reported that the global consumption of BPA was about 8 million tons, and this value was expected to reach 10.6 million tons in 2022 [6]. BPA can transfer to the natural environment, and eventually get into human body through the food chain [7]. The average concentration of BPA detected in surface water is about 100 ng/L, and previous study has shown that BPA has been detected in blood and saliva [8,9]. Thus, there is an urgent need for an effective way to remove BPA from water environment.

Conventional techniques, *i.e.* adsorption, filtration and biodegradation were restricted by a limited removal efficiency and a secondary pollution in the decomposition of BPA [10,11]. To address this issue, the visible-light-driven photocatalytic oxidation processes were presented with the merits of environmental-benign and energy-saving to utilize active species, such as hydroxyl radicals (•OH), for eliminating refractory organic pollutants from water environment [12]. In comparison with traditional hydroxyl radicals, the superoxide radicals ($O_2^{\bullet-}$) and singlet oxygen ($^1O_2$) prefer to attack nucleophiles, therefore $O_2^{\bullet-}$ and $^1O_2$ driven photocatalysis were endowed the capacity of selective oxidation organics with electron-donating groups, such as BPA with –OH and –CH$_3$ groups. Among various semiconductor photocatalysts, Bi-based photocatalysts have gain great interests because of their marvelous photocatalytic activity and favorable band structure to generate various reactive oxygen species (ROS) [13,14]. In particular, bismuth oxide formate (BiOCOOH) only contains “green” elements of C, H and O, and

* Corresponding authors.
*E-mail addresses:* wangweirs@hit.edu.cn (W. Wang), huaiqiu1234@126.com (J. Jia).

https://doi.org/10.1016/j.seppur.2022.122087
Received 24 June 2022; Received in revised form 5 September 2022; Accepted 6 September 2022
Available online 11 September 2022

possesses layered structure with $[Bi_2O_2]^{2+}$ slab and serrated $COOH^-$ [15], which can accelerate the separation of photogenerated carries and avoid the secondary pollution [16]. However, pristine BiOCOOH is still limited by some shortcomings such as only responding to ultraviolet light (wide band gap ( ~ 3.30 eV)) and low photo quantum efficiency [17].

In order to overcome above shortcomings, in our previous study [18], we constructed a hybrid composite by combining BiOCOOH and bismuth oxyiodide (BiOI), and optimized the best proportion of BiOCOOH and BiOI of the sample, namely $BiO(HCOO)_{0.75}I_{0.25}$, which exhibited excellent photocatalytic performance. However, for better practical application, it is still necessary to further improve its photocatalytic activity. Z-scheme photocatalytic system is a two-photon system which consists of photo-reductant, photo-oxidant and electron transport medium. Z-scheme photocatalyst has great advantages in photocatalytic reaction, for example, with the help of two-photon excitation process, the oxidation reaction and reduction reaction can be completed on different photocatalysts, which effectively promotes the separation and migration of photogenerated charges. Additionally, photocatalytic reduction site and photocatalytic oxidation site are on two photocatalysts, respectively, thus, the reduction and oxidation process are separated from each other, which can effectively inhibit the occurrence of reverse reactions. At the same time, the holes in the photo-reductant are recombined with photogenerated electrons from the photo-oxidant of Z-scheme photocatalyst, so the stability of the photocatalytic system is enhanced. Hence, constructing Z-scheme photocatalytic system may be a feasible way since it owns broad spectral response, high stability, high separation efficiency of photoinduced carriers, and strong redox capacity [19–22].

Silver bromide (AgBr) is always considered as an outstanding photocatalyst owing to its strong visible light response and excellent light sensitivity [23,24]. Nevertheless, solo AgBr is easily agglomerated, thus leading to the recession of photocatalytic activity [25]. On this occasion, a suitable substrate may be helpful to disperse AgBr particles from aggregation, and thus enhance the photocatalytic performance.

Hence in this study, we creatively combined AgBr and $BiO(HCOO)_{0.75}I_{0.25}$ to construct a novel Z-scheme $AgBr/BiO(HCOO)_{0.75}I_{0.25}$ heterojunction for photocatalytic elimination of BPA and other four organics, in accordance with its activity, selectivity, and identification of reactive species and key triggers. Meanwhile, the composition, morphology, elemental chemical states and photochemical characteristic of as-prepared photocatalyst were systematically investigated via a series of characterizations. Finally, a probable photocatalytic oxidation mechanism and degradation pathway was proposed for BPA decomposition via $AgBr/BiO(HCOO)_{0.75}I_{0.25}$ composite.

## 2. Experimental section

### 2.1. Preparation of ultrathin $BiO(HCOO)_{0.75}I_{0.25}$ composite nanosheets

$BiO(HCOO)_{0.25}I_{0.75}$ solid solution photocatalyst was fabricated by a simple hydrothermal method according to our previous findings [18] and recorded as BHI-0.75. The detailed preparation process was described in the Supporting Information (Test S1.2).

### 2.2. Preparation of ultrathin $AgBr/BiO(HCOO)_{0.75}I_{0.25}$ nanosheets

0.290 g of prepared BHI-0.75 material (1 mmol) was dispersed in 30 mL water by ultrasound. After 1 mL $AgNO_3$ solution (0.1 M) was added into this mixture with stirring for 10 min, 20 mL solution containing 0.1 mmol NaBr was slowly dropped into the above solution and stirred for 3 h. Finally, an orange sample of 10%AgBr/BHI-0.75 was obtained after washing with deionized water, centrifugation and drying at 60 °C, denoted as 10%ABB (10% represented the molar ratio of AgBr to BHI-0.75). As a control sample, 5%, 20% AgBr/BHI-0.75 and pure AgBr were obtained by changing the proportion of regents, which were denoted as 5%ABB, 20%ABB and AB, respectively.

### 2.3. Evaluation of photocatalytic activity

0.02 g of photocatalyst was dispersed into a 150 mL quartz reactor containing 100 mL BPA solution (10 mg/L) which was equipped with cooling water, and the reaction temperature was maintained at 25 °C. A 300 W xenon lamp source (Beijing Perfectlight, PLS-SXE300D) with a 420 nm cut-off filter was employed as the light source. The vertical distance between the lamp and the liquid level was fixed at 14 cm, and the illumination intensity of the reactor was stabilized at 410 $mW/cm^{-2}$. At certain time intervals, about 2 mL of solution was taken from the reactor to determine the residual concentration of contaminants with a UPLC system (Waters, ACQUITY UPLC H-CLASS). To evaluate the recyclability of the samples, the photocatalyst was washed with deionized water, separated with centrifugation, and dried at 60 °C between each cycle.

More detailed information about materials, characterization of photocatalysts, targeted contaminants measurement and photoelectrochemical measurement were described in Supporting Information (Test S1).

## 3. Results and discussion

### 3.1. Photocatalyst structure and properties

Fig. 1 reveals the XRD patterns of single AgBr, BHI-0.75 and AgBr/BHI-0.75 composites with different proportions. As shown in Fig. 1a, the peaks at 2θ values of 28.8°, 32.5°, 46.5°, 55.6° agreed well with (102), (110), (200), (212) crystal planes of BiOCOOH (PDF NO. 35-0939) [26], and the peak at 31.6° was assigned to the facet (110) of BiOI (PDF NO. 10-0445) [27], suggesting that the BHI-0.75 was hybrid intermediary combining BiOCOOH and BiOI, as reported in our previous work. However, no obvious AgBr characteristic peak was found in AgBr/BHI-0.75 composites (Fig. 1b), this could be attributed to the low content of AgBr as well as its high dispersion on the composites.

The morphology of BHI-0.75 and AgBr/BHI-0.75 photocatalysts were explored by SEM and TEM techniques. As shown in Fig. 2a-b, the pure AgBr displayed smooth spherical structure, and the BHI-0.75 exhibited flower-like spherical structure assembled by abundant nanosheets. While after loading AgBr (Fig. 2c), the AgBr/BHI-0.75 composites displayed a laminated structure, demonstrating that AgBr was intimately decorated on the surface of BHI-0.75 nanosheets. In Fig. 2d-e, the TEM image further disclosed that AgBr nanoparticles were evenly and closely anchored on the surface of BHI-0.75. Additionally, the HRTEM image of the 10%ABB (Fig. 2f) confirmed a close link between AgBr and BHI-0.75. The lattice spacings of 0.267 nm and 0.280 nm referred to (111) and (110) crystal planes of BHI-0.75 [28,29], and the lattice distance of 0.204 nm and 0.336 nm were ascribed to (220) and (111) lattice planes of AgBr [30]. Furthermore, as displayed in Fig. 2g, the EDS mapping images also confirmed that Ag, Br, Bi, I, C and O elements were evenly distributed. The above results provided strong evidence that AgBr/BHI-0.75 heterostructure was successfully fabricated.

The elemental composition and chemical state of 10%ABB composite was further investigated by XPS characterizations. As depicted in Fig. 3a, the peaks located at 367.5 eV and 373.5 eV were belonged to Ag $3d_{5/2}$ and Ag $3d_{3/2}$, respectively, and these peaks could not be further divided, indicating that there was only $Ag^+$ existed in the 10%ABB composite [31,32]. As for $Br_{3d}$ spectrum, the peaks with binding energy of 67.65 eV and 68.75 eV (Fig. 3b) were ascribed to Br $3d_{5/2}$ and Br $3d_{3/2}$, respectively [33]. The peaks of Bi 4f locating at 159.08 eV and 164.36 eV were belonged to Bi $4f_{7/2}$ and Bi $4f_{5/2}$, respectively (Fig. 3c) [28]. With regard to I 3d spectrum, the peaks located at 630.4 eV and 618.84 eV were classified to I $3d_{5/2}$ and I $3d_{3/2}$, respectively (Fig. 3d) [34,35]. In the C1s spectrum (Fig. 3e), peak at 285 eV was indexed to C-C binding, and another peak at 287.58 eV referred to carboxyl group [36]. XPS of O

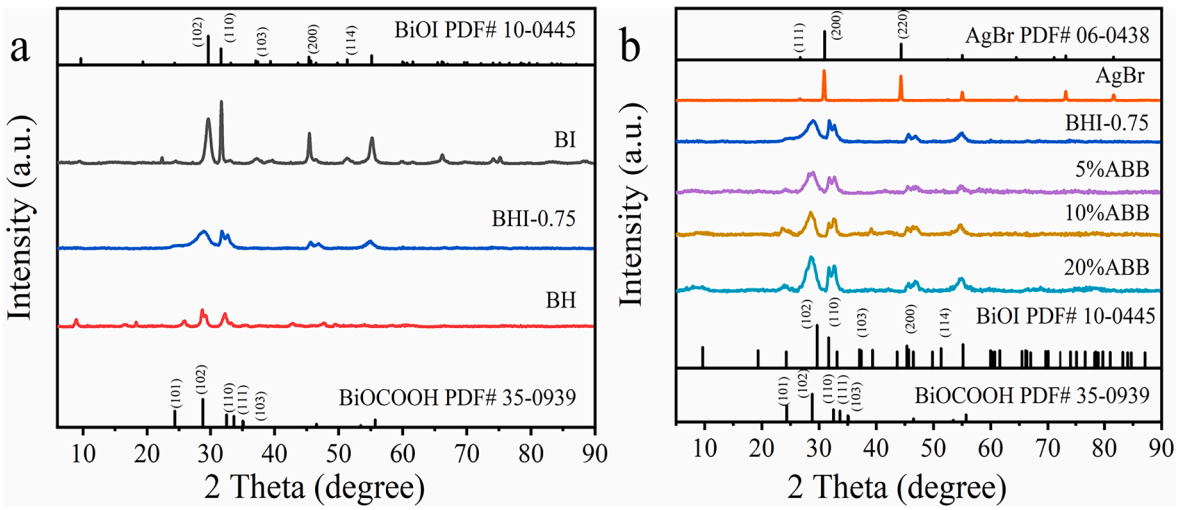


**Fig. 1.** (a) XRD patterns of BI, BH and BHI-0.75. (b) XRD patterns of AgBr, BHI-0.75 and AgBr/BHI-0.75 composites.

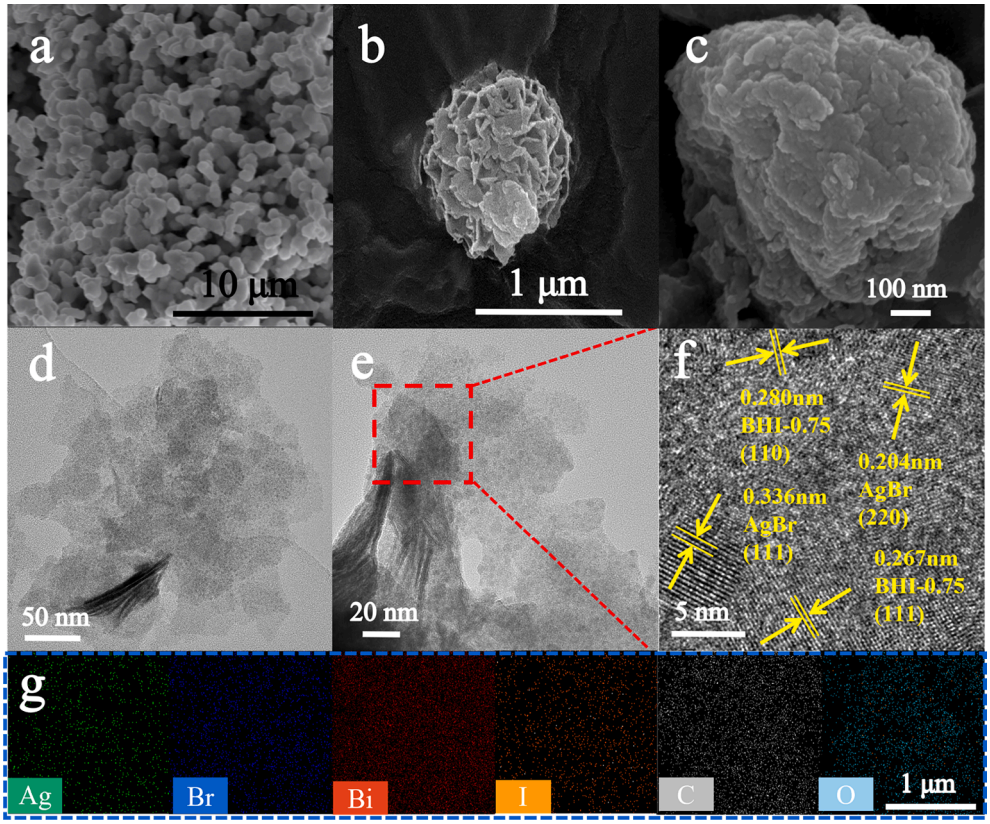


**Fig. 2.** The SEM image of (a) pure AgBr, (b) ultrathin BHI-0.75 nanosheets, and (c) 10% AgBr/BHI-0.75 nanosheets. (d-f) TEM and HRTEM images of 10% AgBr/BHI-0.75 nanosheets. (g) The EDS mapping images of 10%ABB nanosheets.

1s (Fig. 3f) were divided into three peaks, which were located at 529.72, 530.98 and 532.48 eV, corresponding to Bi-O, O-H and -COOH, respectively [37,38]. Notably, some peaks of these above elements in AgBr/BHI-0.75 composite shifted compared with pristine AgBr or BHI-0.75, evidencing the occurrence of charge redistribution after assembling AgBr on the surface of BHI-0.75. All the findings confirmed that the AgBr/BHI-0.75 composites were successfully fabricated. Moreover, compared to the peaks in the Ag 3d spectra of pristine AgBr, the binding energies of XPS spectra of Ag 3d are shifted to the higher values on 10% ABB. Compared to the peaks of pristine BHI-0.75, the peaks in the Bi 4f, I 3d, C1s, and O 1s are shifted to low values on 10%ABB. In general, binding energy is negatively related to surface electron density. Therefore, the opposite shift direction of the binding energy for the elements of AgBr and BHI-0.75 implied the electron transfer from AgBr to BHI-0.75 [39,40].

### 3.2. Photocatalytic performance analysis

#### 3.2.1. Degradation kinetic and stability

The photocatalytic performance of the as-prepared samples was evaluated by employing BPA as the target pollutant under visible light irradiation. In the dark condition, BPA and photocatalyst suspensions

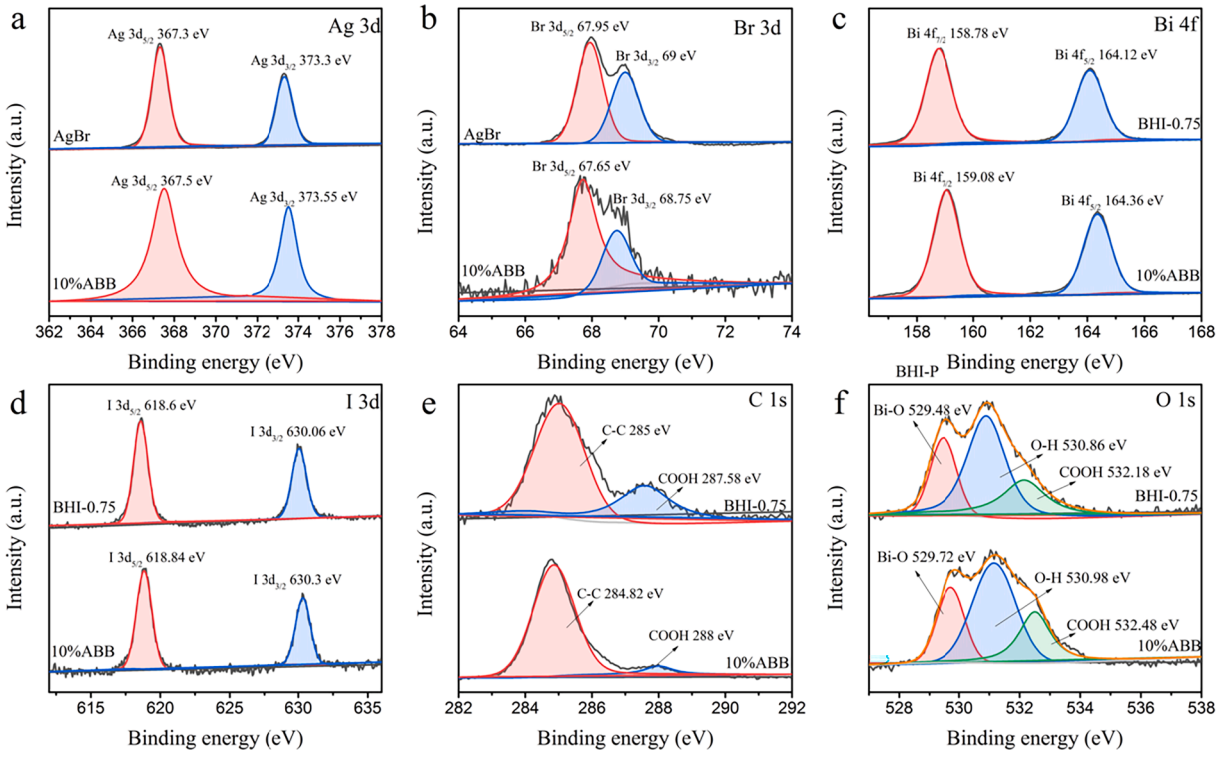


**Fig. 3.** The high resolution XPS spectra of BHI-0.75, AgBr and 10%ABB composites: (a) Ag 3d, (b) Br 3d, (c) Bi 4f, (d) I 3d, (e) C 1s and (f) O 1s.

were observed to reach an absorption–desorption equilibrium at 15 min, and all samples showed weak BPA adsorption capacity (Fig. S1). When the light was switched on, as displayed in Fig. 4a, the BPA concentration barely fluctuated in the blank group during 30 min reaction time, excluding the self-decomposition of BPA. Conversely, the degradation efficiency of BPA by AgBr and BHI-0.75 was 67.4%, and 97% within 30 min, respectively. It was clearly to see that the BPA removal efficiency further improved when 5%ABB and 10%ABB were added into the system. Specially, 10%ABB exhibited a better photocatalytic performance than that of 5%ABB, which could completely remove BPA within 25 min. The improved photocatalytic performance of ABB composites could be ascribed to the construction of heterojunction structure, which not only enhanced the light harvest capability, but also accelerated the separation rate of photo-generated charges. However, the BPA removal

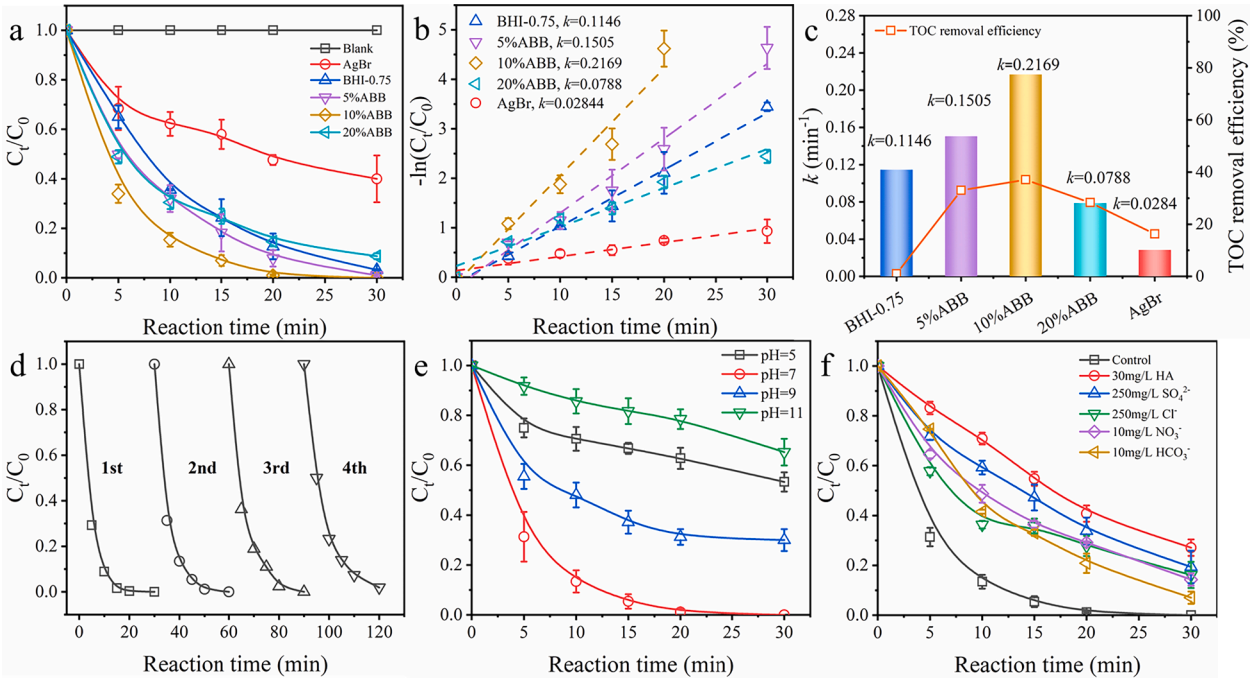


**Fig. 4.** (a) BPA degradation in visible light over different samples. (b) Pseudo first-order kinetic fitting, (c) the determined apparent rate constants (k) and TOC removal efficiencies of ABB samples. (d) Reusability of photocatalysis degradation of BPA. (e) The effect of pH on BPA degradation in 10%ABB/VL system. (f) The effects of inorganic anions and HA on BPA degradation in 10%ABB/VL system.

efficiency became declined when the amount of decorated AgBr increased to 20%. This might be due to the fact that the excess AgBr yielded light shielding effect, resulting in inadequate light absorption of the composite [41].

The kinetics of BPA degradation in all systems were fitting well the pseudo first-order model. As displayed in Fig. 4b, 10%ABB displayed the highest kinetic rate constant ($k = 0.2135\ min^{-1}$), which was 1.4, 1.9, 2.7 and 7.5 times higher than that of 5%ABB ($0.1505\ min^{-1}$), BHI-0.75 ($0.1146\ min^{-1}$), 20%ABB ($0.0788\ min^{-1}$) and AgBr ($0.0284\ min^{-1}$), respectively. The TOC removal performance of the as-prepared samples was also explored (Fig. 4c), and the results were consistent with the trend of kinetics constant, namely that the 10%ABB showed the best TOC removal performance (37.1%) among all the five samples, indicating its good mineralization ability.

The stability of 10%ABB was also evaluated. As shown in Fig. 4d, after four cycles of use, the BPA degradation rate could still achieve 100%. Meanwhile, after four reuses, the mass loss of 10%ABB was 14%, and only 0.0006 mg/L $Ag^+$ were detected in reaction solution. It was worth noting that in the XRD spectra of fresh and 4th reused 10%ABB (Fig. S2a), the peak intensity of 4th repeated 10%ABB were slightly stronger than that of the fresh sample, and the peak pattern became sharp. According to the Scherrer formula, the grain size of 10%ABB became larger after 4th repeated use. Moreover, some small peaks were also found in the XRD spectra of the recycled sample. In view of this phenomena, it was speculated that some degradation intermediates might adhere on the surface of 10%ABB during the reaction process, which not only resulted in larger grains of the sample, but also brought some impurities, thus leading to the sharper peak patterns and some small miscellaneous peaks. Even so, the 2θ value of several major peaks of the sample have barely changed after 4th cycling, indicating the crystal phase of 10%ABB is stable. In addition, it was found that there was almost no difference between the XPS spectra and SEM images of fresh and 4th reused 10%ABB (Fig. S2b-d). The above results suggested that the 10%ABB have good stability both in terms of degradation performance and physicochemical structure.

### 3.2.2. Effects of initial BPA concentration

Effects of initial concentration of BPA on the degradation rate of the system was explored by varying BPA concentrations from 5 mg/L to 20 mg/L and maintaining the amount of 10%ABB (0.2 g/L) at pH 7. As shown in Fig. S3, with the increase of BPA concentration, the BPA degradation performance exhibited a downward trend. This could be ascribed to that the amount of photocatalyst in the system was fixed, this determined that the amount of reactive species in the system was also fixed. Therefore, there were no enough reactive species to attack the excess BPA. Besides, the increase of BPA concentration might bring about the increase of degradation intermediates, which lead to a competitive effect between BPA and the intermediates [42]. However, based on kinetic rate constant ($k$) of different concentrations of BPA (Fig. S3), although the $k$ of 5 mg/L was 2.1 times greater than that of 10 mg/L, the $k$ of 10 mg/L was 6.3 times greater than that of 15 mg/L. Therefore, when the concentration of BPA is 10 mg/L, the system has the best photocatalytic performance.

### 3.2.3. Effects of reaction pH

The effect of initial pH on photocatalytic performance of the system was carried out with the pH range from 5 to 11. As shown in Fig. 4e, the system obtained the best oxidation performance at pH 7, acidic and alkaline conditions were not conducive to BPA degradation. This could be explained by that the charge on the surface of photocatalyst is pH-dependent, and in general, the heterojunction is positively charged under acidic conditions and negatively charged under alkaline conditions [43], The measured zeta potential of 10%ABB at pH 5, 7, 9 and 11 was 3.4 eV, 1.8 eV, −2.7 eV and −7.3 eV, respectively. Based on previous study, BPA exists as a cation in acidic conditions, and exists as an anion under neutral and alkaline conditions [44,45]. Therefore, under acidic condition and alkaline conditions, the electrostatic repulsion between photocatalyst and BPA hampered the reaction process, while, at neutral condition, electrostatic attraction promoted the reaction of the system.

### 3.2.4. Effects of inorganic anions

Inorganic anions and natural organic matter (NOM) in water may affect the oxidation capacity of the photocatalytic system. Thus, it is necessary to investigate the effects of inorganic anions and NOM in water on BPA degradation in the 10%ABB/VL system. According to the surface water standard (GB3838-2002), four common inorganic salts ($Na_2SO_4$ (250 mg/L), NaCl (250 mg/L), $NaNO_3$ (10 mg/L) and $NaHCO_3$ (10 mg/L)) and HA (30 mg/L) were chosen and introduced to the system. As shown in Fig. 4f, when these inorganic anions and NOM added to the system, the degradation rate of BPA dropped from 100% to 72.9%, 80.7%, 83.9%, 85.7% and 93.0%, respectively. The inhibitory effect of inorganic anions usually can be classified into two reasons: competitive adsorption on active sites and quench effect of generated $^{\bullet}OH$ [46]. However, Section 3.4.1 has clarified that the $O_2^{\bullet-}$ played the dominant role in the 10%ABB/VL system, and $^{\bullet}OH$ were formed in small amounts. Thus, the inhibitory effect caused by inorganic anions was mainly ascribed to the competitive adsorption, resulting in a portion of catalytic active sites were occupied. Meanwhile, HA could consume the reactive species including $^{\bullet}OH$ and $O_2^{\bullet-}$, and induce the photo shielding effect, thus decrease the BPA degradation efficiency [47]. Even so, the system could still achieve a relatively satisfactory degradation rate within 30 min (over 70%), manifesting the AgBr/BHI-0.75 system possesses a high resistance to the complex water matrix.

## 3.3. Selective oxidation of organic contaminants

The selective oxidation of organic contaminants is always a challenge for photocatalytic advanced oxidation processes (AOPs). In this work, five frequently detected organic pollutants including BPA, parachlorophenol (4-CP), paranitrophenol (4-NP), 4-hydroxybenzaldehyde (p-HBA) and sulfamethoxazole (SMX) in wastewater were selected to investigate the selective oxidization ability of the AgBr/BHI-0.75 system. It can be clearly seen from Fig. 5a that the 10%ABB/VL system exhibited an obvious difference in the degradation capabilities of these five organic pollutants. The degradation efficiencies and corresponding kinetic constants followed the order: BPA > p-HBA > SMX > 4-CP > 4-NP (Fig. 5a-b), which was possibly ascribed that the substituent differences affected the antioxidant electrochemical character of organic compounds in photocatalytic AOPs.

As discussed in Section 3.4.1, $O_2^{\bullet-}$, $h^+$, $^1O_2$ and $^{\bullet}OH$ participated in the 10%ABB/VL system. Except $^{\bullet}OH$ as a nonselective radical, the other active species are more likely to attack nucleophiles [48,49], namely the organics which contain electron donating groups (EDGs) such as $–CH_3$ and –OH groups are more easily degraded by $O_2^{\bullet-}$, $h^+$ and $^1O_2$. On the contrary, the organics which contain electron withdrawing groups (EWGs) such as –COOH and $–NO_2$ groups, were hard to degraded by these three species. As depicted in Fig. 5a, BPA was the most easily decomposed in the 10%ABB/VL system since it contains $–CH_3$ and –OH groups. While for 4-CP and 4-NP, since they have electron withdrawing groups like –Cl and $–NO_2$ groups, thus low degradation rates were obtained. Furthermore, ionization potential (IP) is regard as an organic molecular descriptor related to functional groups, which was reported closely correlated to the reaction rates in several oxidation system [50–52]. To be more specific, EDGs can lower the IP value of the organics, while EWGs have an opposite effect. By plotting the relationship between IP value and kinetic constant ($k$) of different organics degradation in the 10%ABB/VL system (Fig. 5b), it was demonstrated that organics with a high IP value generally possessed a low reaction rate. Nevertheless, p-HBA showed a higher oxidizing capacity than expected, which was owing to the strong electrostatic attraction between the ABB surface and p-HBA. The dissociation constant of p-HBA is smallest ($pK_a$

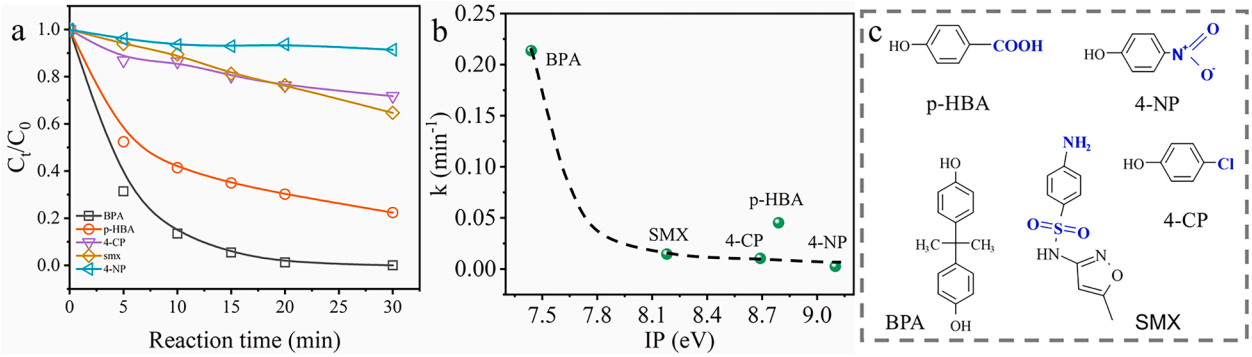


**Fig. 5.** (a) Different pollutants degradation in 10%ABB/VL system. (b) The corresponding kinetic fitting curves. (c) Structural formulas of different organic compounds.

= 4.57) among the five contaminants, therefore under the neutral condition, p-HBA exhibits electronegative state. According that the zeta potential of AgBr/BHI-0.75 is 1.8 eV at pH = 7, the sample surface is positive charged, so the electrostatic attraction effect enhances the oxidation reaction probability of p-HBA. The above discussion disclosed that 10%ABB/VL system enabled to decompose a wide range of organics, and also possessed a high selective oxidation of organic pollutants with electron donating groups or low IP value.

### 3.4. Photocatalytic oxidation mechanism insights

#### 3.4.1. Identification of reactive species

To identify the reactive species involved in the 10%ABB/VL system, the ESR measurements were performed. As shown in Fig. 6a-d, in the dark condition, there was no characteristic peaks of any reactive species were detected. However, when the light was switched on, the characteristic peaks of $^{\bullet}OH$, $O_2^{\bullet-}$, $^1O_2$ and $h^+$ appeared within 1 min illumination, and the peak intensities boosted with the time prolonged to 3 min, indicating that $^{\bullet}OH$, $O_2^{\bullet-}$, $^1O_2$ and $h^+$ might be involved in the 10%ABB/VL system.

Then, the radical quenching experiments were conducted to further clear the role of reactive species played during BPA degradation process, where the *tert*-butanol (TBA), ascorbic acid (AA), furfuryl alcohol (FFA) and sodium oxalate (SO) were employed as the scavenger of $^{\bullet}OH$, $O_2^{\bullet-}$, $^1O_2$, and $h^+$, respectively. As shown in Fig. 6e, when 5 mM TBA was added into the reaction system, the degradation of BPA was slightly suppressed, manifesting that $^{\bullet}OH$ played a tiny part during BPA degradation process. When 5 mM FFA and 5 mM SO were added, the BPA degradation efficiency decreased from 100% to 74.8% and 44.9%, respectively, indicating that $^1O_2$ and $h^+$ played a more essential role than that of $^{\bullet}OH$. While, when 5 mM AA was introduced to the reaction system, the degradation of BPA was almost completely inhibited, demonstrating that $O_2^{\bullet-}$ play the main role in BPA degradation process. Therefore, it could be concluded that $^{\bullet}OH$, $O_2^{\bullet-}$, $^1O_2$, and $h^+$ were all involved in the BPA removal process, and the contribution of these four reactive species followed this order: $O_2^{\bullet-} > h^+ > {}^1O_2 > {}^{\bullet}OH$.

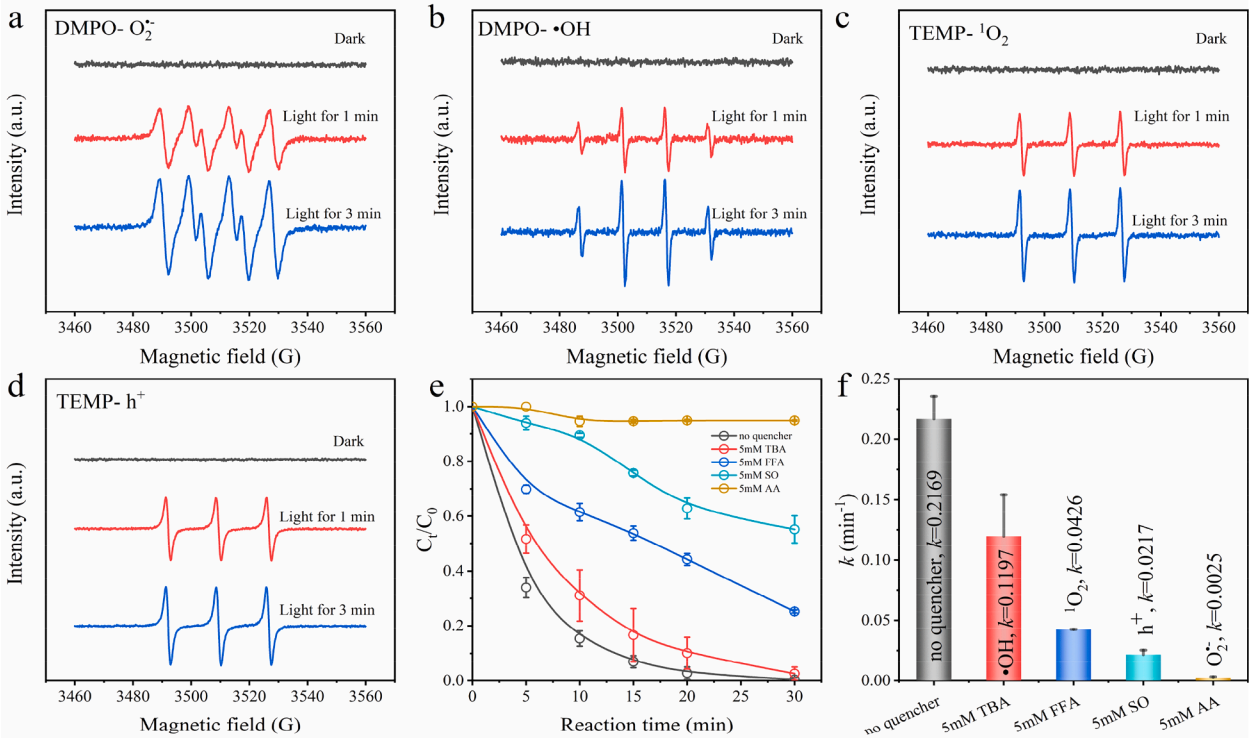


**Fig. 6.** (a-d) EPR spectra of $O_2^{\bullet-}$, $^{\bullet}OH$, $^1O_2$ and $h^+$ in different systems. (e) The degradation curves of 10%ABB/VL system with addition of different scavengers, and (f) the corresponding *k* values.

### 3.4.2. Insights into photoelectric property

The optical properties of AgBr, BHI-0.75 and 10%ABB were studied using UV– vis DRS technology. As shown in Fig. 7a, the 10%ABB composites exhibited an obvious absorption in the visible light spectrum, and the absorption edge was intermediate between two monocomponents. Based on Tauc's plots, the corresponding band gap energy (Eg) of the three samples was calculated to be 2.55, 1.78 and 1.82 eV for AgBr, BHI-0.75 and 10%ABB, respectively (Fig. 7b). In addition, VB-XPS was performed to determine the band structure of the photocatalysts. In Fig. 7c, valence bands of AgBr and BHI-0.75 positioned at 2.33 and 0.7 V, respectively. According to the empirical formula ($E_{CB} = E_{VB}$-$E_g$), the conduction band of AgBr and BHI-0.75 was −0.22 and −1.08 V, respectively. By matching the energy band (Fig. 7d), a heterostructure is very possible to be constructed between AgBr and BHI-0.75.

To investigate the separation and migration properties of photogenerated electron-hole pairs of three samples, a series of photoelectric performance characterization were performed. Firstly, the photoluminescence (PL) spectra was conducted. Generally, in the PL spectra, the lower fluorescence manifested the faster separation and lower recombination rate of the photo-generated carriers, which signified the excellent photocatalytic performance [18]. Fig. 8a demonstrates the PL spectra of AgBr, BHI-0.75 and 10%ABB at the excitation wavelength of 250 nm. Compared with AgBr and BHI-0.75, 10%ABB composite exhibited an obviously depressed PL intensity, indicating that the heterojunction constructed between BHI-0.75 and AgBr was beneficial to the separation of photo-generated carriers and restrain the recombination of electron-hole pairs.

Then, the transient photocurrent response (TPR) tests was carried out to further investigate the separation and migration capability of the photo-generated carriers of the three samples. As shown in Fig. 8b, when the light was turned on, all the three samples exhibited certain photocurrent responses. Obviously, the photocurrent intensity of 10%ABB was higher than that of AgBr and BHI-0.75, implying that the heterojunction between AgBr and BHI-0.75 could promote the migration of photo-generated carriers. Additionally, from the electrochemical impedance spectroscopy (EIS) Nyquist curves (Fig. 8c), it could be seen that 10%ABB exhibited the smallest arc radius among three photocatalysts. Generally, in EIS characterization, the smaller the arc radius means a smaller charge transfer resistance, namely a more efficient separation of photo-generated carriers [53]. The TPR and EIS results appear the similar result like PL spectra, and were also consistent with the photocatalytic degradation performance. In addition, time-resolved PL was used to study the charge life of the photocatalysts. As shown in Fig. 8d, the fluorescence lifetimes of BHI-0.75, AgBr and 10%ABB were 1.63 ns, 1.81 ns and 1.18 ns, respectively. The reduced carrier lifetime also indicated the accelerated process of photoexcitation dissociation [54], which was consistent with the corresponding photoelectrochemical results.

### 3.4.3. Photo-deposition experiments

To further confirm the photocatalysis mechanism, photo-deposition experiments were carried out to determine the generation sites of photogenerated carriers. $H_2PtCl_6$ and $MnCl_2$ were employed to confirm photogenerated electrons and holes, respectively. When using ascorbic

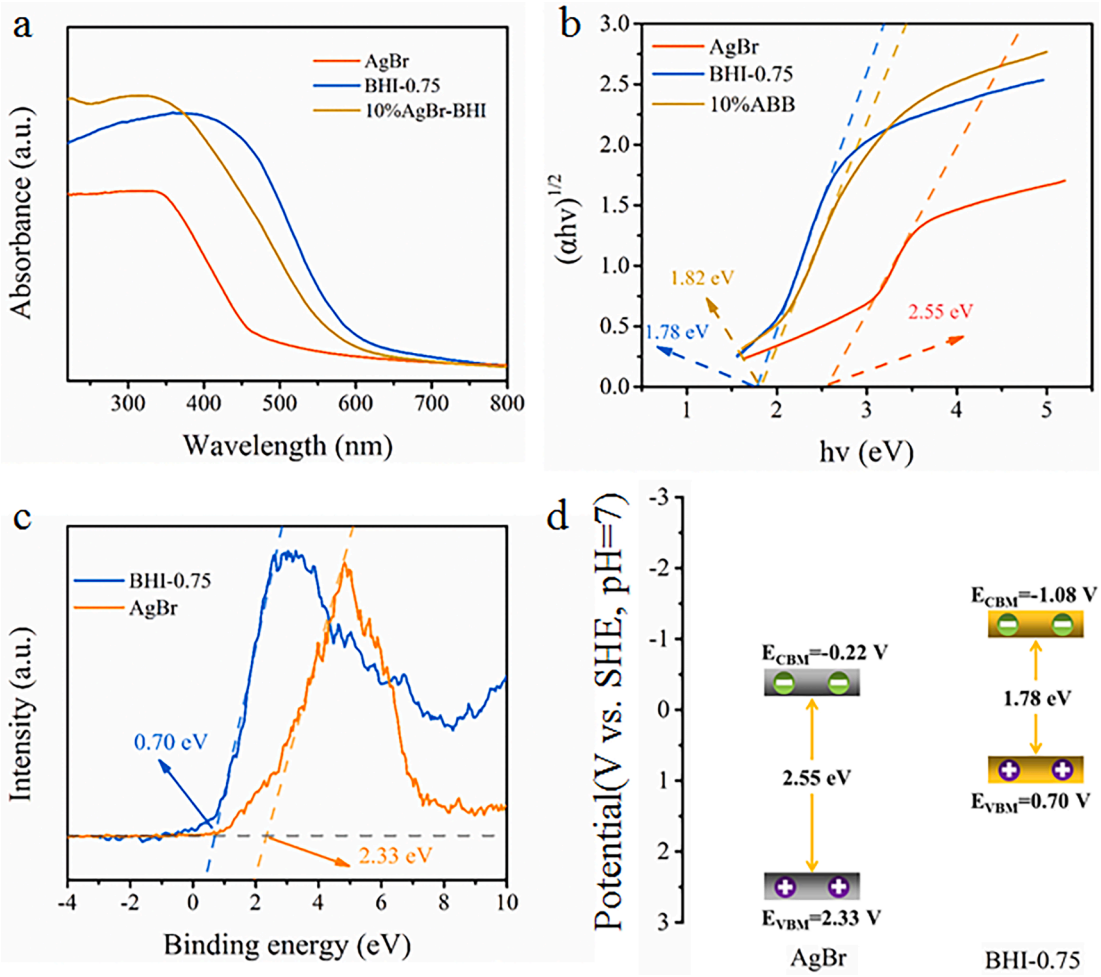


**Fig. 7.** (a) UV–vis diffuse reflection spectra of BHI-0.75, AgBr and 10%ABB. (b) The bandgap value, estimated by a related curve of $(\alpha h\nu)^{1/2}$ versus photon energy plotted. (c) VB-XPS spectra of BHI-0.75, AgBr and 10%ABB. (d) The band position schematic of BHI-0.75, AgBr and 10%ABB.

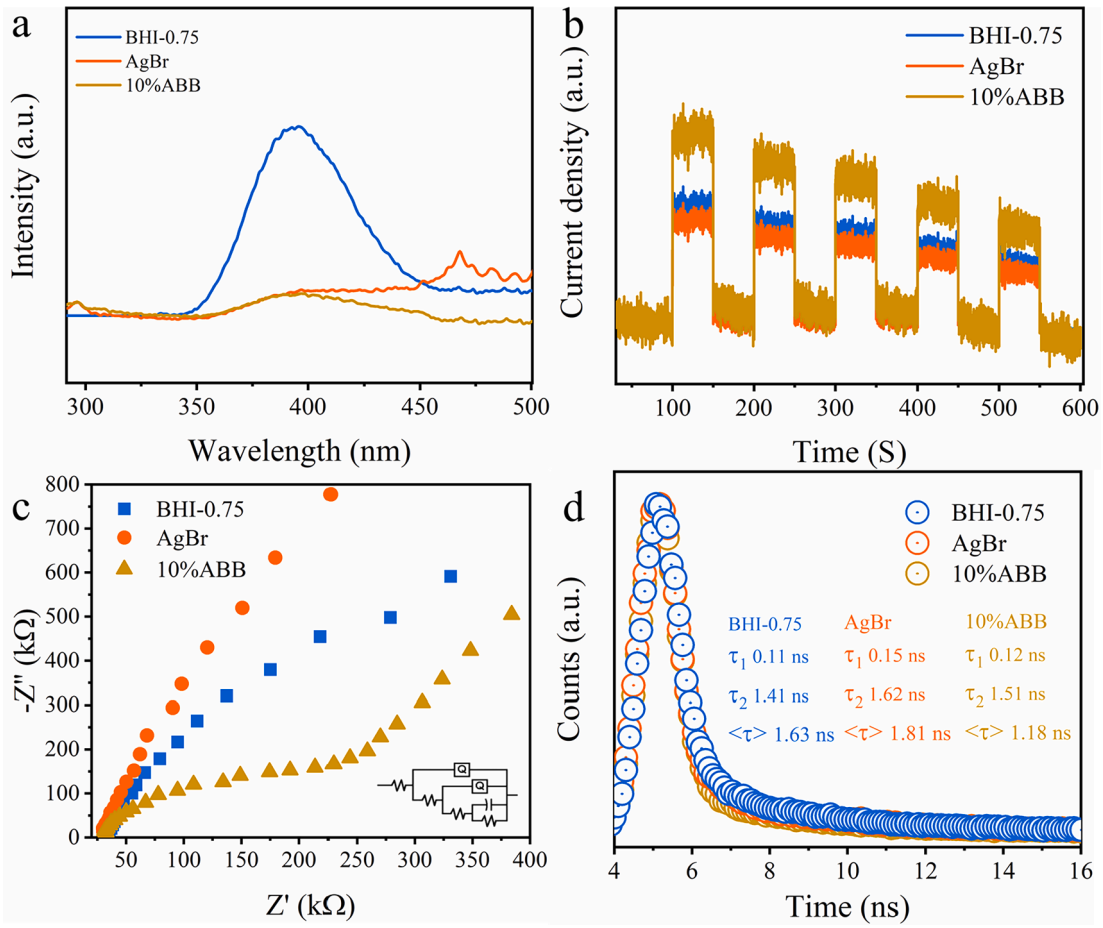


**Fig. 8.** (a) PL spectra. (b) Transient photocurrent responses. (c) Electrochemical impedance spectroscopy of different samples. (d) Time-resolved transient PL decay spectroscopy of BHI-0.75, AgBr and 10%ABB.

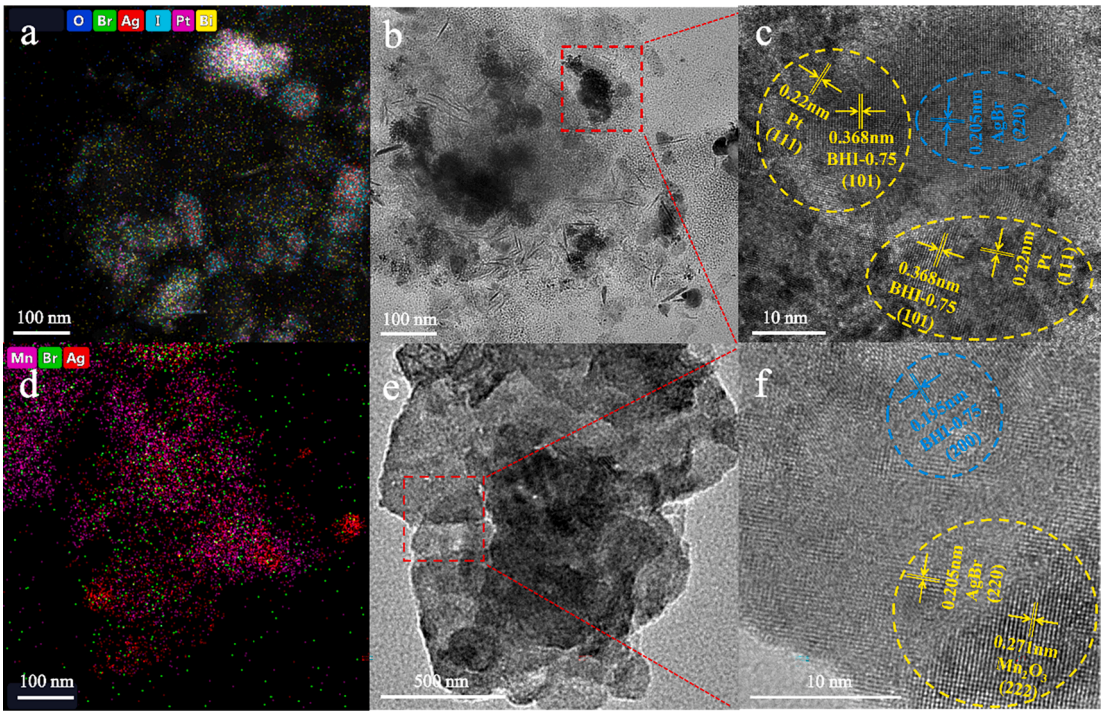


**Fig. 9.** Anisotropic migration of photogenerated carriers. EDS mapping and high resolution TEM of Pt (a-c) and $Mn_2O_3$ (d-f) photodeposition on 10%ABB nanosheets.

acid as the hole scavenger, $Pt^{4+}$ could be reduced to Pt by photoinduced electrons. While, when employing $NaIO_3$ as the electron scavenger, $Mn^{2+}$ could be oxidized to $Mn_2O_3$ by the holes. In this way, photogenerated electrons and holes generation sites of 10%ABB sample can be identified by exploring the deposition sites of Pt and $Mn_2O_3$. As depicted in Fig. 9, Pt particles were deposited on BHI-0.75 (Fig. 9a). Additionally, in the HRTEM image, it could be seen that Pt (1 1 1) facet was deposited on the edge of BHI-0.75 (1 0 1) facet (Fig. 9b-c), indicating that the photogenerated electron migrate to the BHI-0.75 for metal reduction. Similarly, it was also found that $Mn_2O_3$ (2 2 2) facet was deposited on the edge of AgBr (2 2 0) facet, suggesting that the holes tend to migrate to AgBr. This is consistent with the charge transfer mechanism of Z-scheme heterojunction, thus it can be concluded that the electron transfer mechanism of 10%ABB is Z-type heterojunction [55–57].

### 3.4.4. Photocatalytic mechanism

As discussed above, a conventional type II heterojunction model was tentatively proposed for AgBr/BHI-0.75 composites (Fig. 10a). As depicted in Fig. 7d, the $E_{CB}$ and $E_{VB}$ of BHI-0.75 were −1.08 and 0.7 eV, and the $E_{CB}$ and $E_{VB}$ of AgBr were −0.22 and 2.33 eV, respectively. When BHI-0.75 and AgBr were excited by visible light, electrons would migrate from BHI-0.75 (CB) to AgBr (CB) due to the more negative CB potential of BHI-0.75 than that of AgBr, and the holes of AgBr (VB) would transfer to BHI-0.75 (VB) because of the more positive VB potential of AgBr than that of BHI-0.75. Since the CB potential of AgBr (−0.22 eV) were more positive than that of $O_2/O_2^{\bullet-}$ (−0.33 eV vs NHE), electrons in the CB of AgBr could not reduce $O_2$ into $O_2^{\bullet-}$. At the same time, holes in the VB of BHI-0.75 could not oxidize $H_2O$ into $^{\bullet}OH$ because of the VB potential of BHI-0.75 (0.7 eV) was more negative than $H_2O/^{\bullet}OH$ potential (1.99 eV vs. NHE). In this case, $O_2^{\bullet-}$ and $^{\bullet}OH$ would not be formed in the system, this is not consistent with the results of quenching experiment and ESR characterization. Thus, the type II heterojunction model is not applicable to 10%ABB composite in this study.

According to previous studies [30,34], the direction Z-scheme system may be suitable for this AgBr/BHI-0.75/VL system (Fig. 10b). When 10%ABB was illuminated with visible light (Eqs. 1–2), due to the more positive VB potential of AgBr (2.33 eV) than that of $H_2O/^{\bullet}OH$ (1.99 eV vs. NHE), $^{\bullet}OH$ was produced (Eq. (3)) [58]. And because the CB potential of BHI-0.75 (−1.08 eV) is more negative than that of $O_2/O_2^{\bullet-}$ (−0.33 eV vs NHE), $O_2^{\bullet-}$ could be effectively produced (Eq. (4)). In this way, photogenerated electron-hole pairs were effectively separated and endowed $h^+$ sufficient oxidation capacity for the BPA direct oxidation. Moreover, $^1O_2$ would be generated by deriving from $O_2^{\bullet-}$ (Eqs. 5–6) [59]. Finally, $O_2^{\bullet-}$, $^{\bullet}OH$, $h^+$ and $^1O_2$ all contributed to the BPA degradation (Eq. (7)). The whole process conforms to the natural Z-scheme photocatalytic system, which promotes the separation of photoexcited carriers and further improves the photocatalytic ability.

$$\text{BHI-0.75} + h\nu \rightarrow e_{CB}^- + h_{VB}^+ \quad (1)$$

$$\text{AgBr} + h\nu \rightarrow e_{CB}^- + h_{VB}^+ \quad (2)$$

$$h_{VB}^+ \text{ (AgBr)} + H_2O \rightarrow {}^{\bullet}OH \text{ (AgBr)} + H^+ \quad (3)$$

$$e_{CB}^- \text{ (BHI-0.75)} + O_2 \rightarrow O_2^{\bullet-} \text{ (BHI-0.75)} \quad (4)$$

$$O_2^{\bullet-} + H_2O \rightarrow {}^{\bullet}HOO + OH^- \quad (5)$$

$$O_2^{\bullet-} + {}^{\bullet}HOO \rightarrow {}^1O_2 + HOO^- \quad (6)$$

$$O_2^{\bullet-}/{}^{\bullet}OH/h^+/{}^1O_2 + \text{BPA} \rightarrow CO_2 + \text{intermediate} \quad (7)$$

### 3.4.5. The degradation pathways of BPA

LC-MS/MS tests were conducted to clear the BPA degradation pathway and intermediates in 10%ABB/VL system. Fig. 11 depicts that there were nine degradation intermediates were identified, and the corresponding MS/MS spectra and chemical structure were shown in Fig. S4 and Table S2. According to these results and previous literatures, there were two degradation pathways of BPA existed in 10%ABB/VL system: (i) β-scission [60] and (ii) C-C cleavage [61]. As shown in Fig. 11, β -scission mechanism could convert BPA to P1 and P2, while C-C cleavage could decompose BPA to produce P3, P4 and P5. Then, these products would go through ring-opening reactions, and further converted to P6-P9 [62,63]. Finally, under the continuous action of the reactive species in the system, these products are eventually converted to carbon dioxide and water.

## 4. Conclusion

In this study, a Z-scheme visible-light photocatalyst AgBr/BiO$(HCOO)_{0.75}I_{0.25}$ was successfully fabricated for efficient elimination of organic contaminants. The optimal loading ratio of AgBr was 10 wt%, which could remove BPA completely within 25 min with a kinetic constant of 0.2135 $min^{-1}$, much higher than that of solo AgBr (1.9 folds) and BHI-0.75 (7.5 folds), suggesting that the construction of Z-scheme structure greatly improved the photocatalytic performance of catalysts. The quenching tests and ESR characterization disclosed that both superoxide radical ($O_2^{\bullet-}$) and non-radical ($^1O_2$ and $h^+$) were primary active species, which were more likely to attack nucleophiles. Therefore, this AgBr/BiO$(HCOO)_{0.75}I_{0.25}$/VL system preferred to degrade aromatics with electron donating groups, while was relatively debilitated for organics with electron withdrawing groups. Although inorganic anions and natural organic matter inhibit the oxidative degradation of the system to varying degrees, the system could still reach a satisfactory result. We believe this study will open a new road for selective photocatalytic degradation depending on the eletrophilicity and nucleophilicity properties of the ROS and pollutants.

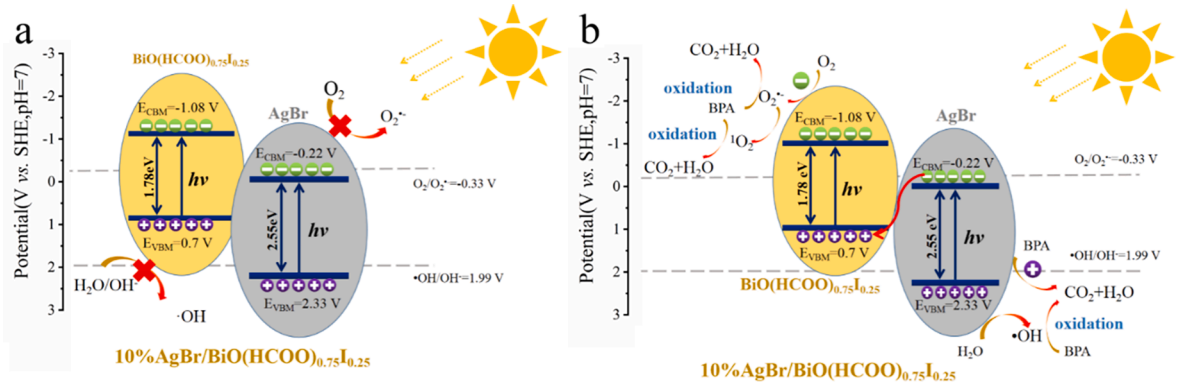


**Fig. 10.** Proposed possible mechanism for BPA degradation in 10%ABB system based on the (a) conventional type II heterojunction and (b) the direction Z-scheme heterojunction.

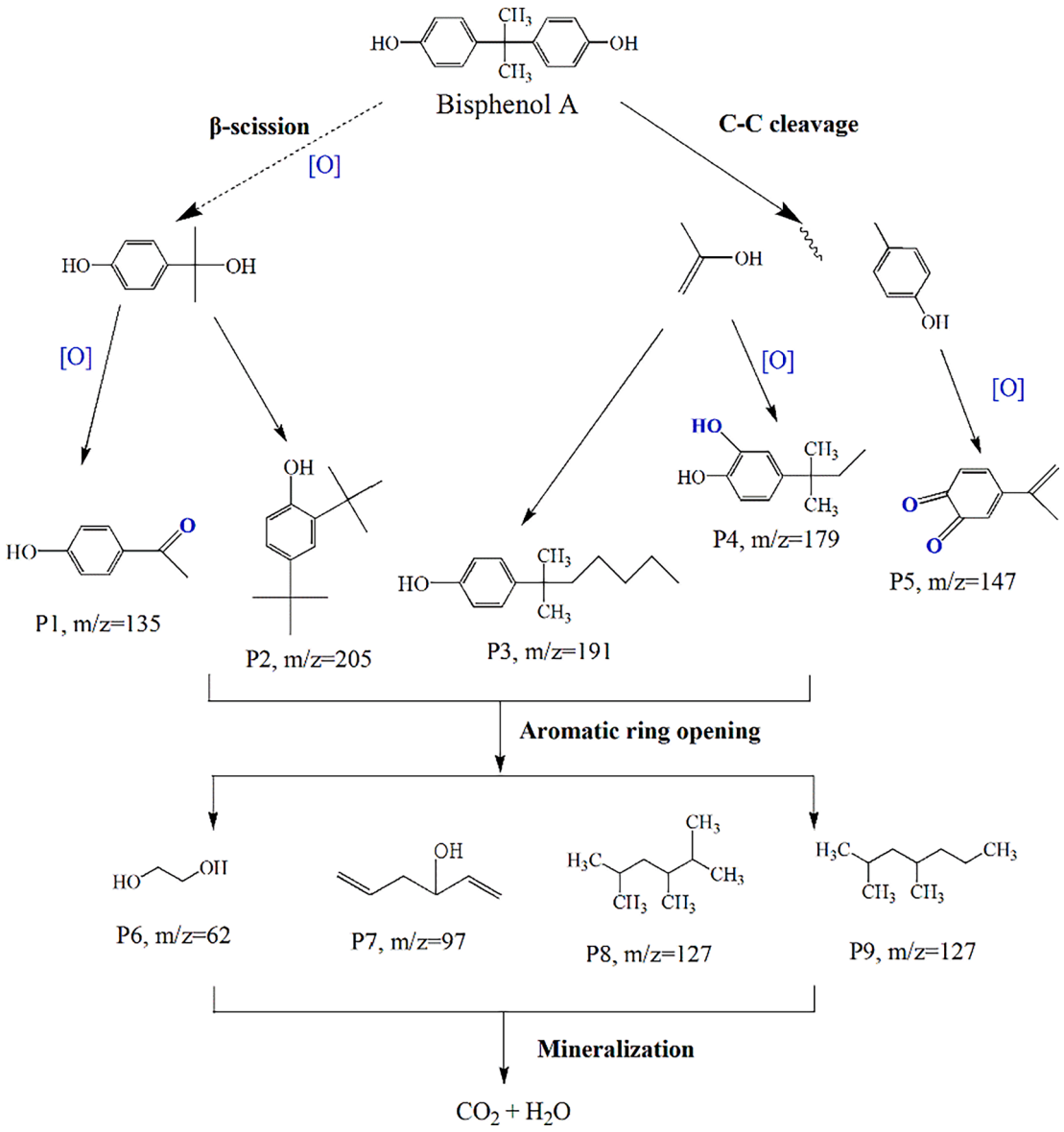


**Fig. 11.** The degradation pathways of BPA in 10%ABB/VL system.

*CRediT authorship contribution statement*

**Qiao Wang:** Methodology, Formal analysis, Writing – review & editing, Funding acquisition. **Yiting Cao:** Investigation, Data curation, Visualization. **Meirui Yu:** Investigation, Data curation. **Guanheng Lv:** Investigation, Data curation, Visualization. **Chuyi Zhang:** Investigation, Data curation. **Wei Wang:** Conceptualization, Supervision, Writing – review & editing. **Jialin Jia:** Methodology, Supervision, Writing – original draft. **Zhihong Wang:** Writing – review & editing.

## Declaration of Competing Interest

The authors declare that they have no known competing financial interests or personal relationships that could have appeared to influence the work reported in this paper.

## Acknowledgements

The authors gratefully acknowledge the Open Project of State Key Laboratory of Urban Water Resource and Environment, Harbin Institute of Technology, China (Grant No. HC202154), the National Natural Science Foundation of China (Grant No. 22006022), and the Science and Technology Project of Guangzhou, China (Grant No. 202102020348). We would like to thank Analysis and Test Center of Guangdong University of Technology for UPLC and UPLC/MS/MS analyses.

## Appendix A. Supplementary data

Supplementary data to this article can be found online at https://doi.org/10.1016/j.seppur.2022.122087.

## References

[1] D. Chen, K. Kannan, H. Tan, Z. Zheng, Y.L. Feng, Y. Wu, M. Widelka, Bisphenol analogues other than BPA: Environmental occurrence, human exposure, and toxicity-A review, Environ. Sci. Technol. 50 (2016) 5438–5453.
[2] F.M. Mpatani, R. Han, A.A. Aryee, A.N. Kani, Z. Li, L. Qu, Adsorption performance of modified agricultural waste materials for removal of emerging micro-contaminant bisphenol A: A comprehensive review, Sci. Total Environ. 780 (2021) 146629.
[3] L. Niu, S. Zhang, S. Wang, L. An, K. Manoli, V.K. Sharma, X. Yu, M. Feng, Overlooked environmental risks deriving from aqueous transformation of bisphenol alternatives: Integration of chemical and toxicological insights, J. Hazard. Mater. 427 (2022), 128208.

[4] R. Banaderakhshan, P. Kemp, L. Breul, P. Steinbichl, C. Hartmann, M. Fuerhacker, Bisphenol A and its alternatives in Austrian thermal paper receipts, and the migration from reusable plastic drinking bottles into water and artificial saliva using UHPLC-MS/MS, Chemosphere 286 (2022), 131842.

[5] C.J. Catenza, A. Farooq, N.S. Shubear, K.K. Donkor, A targeted review on fate, occurrence, risk and health implications of bisphenol analogues, Chemosphere 268 (2021), 129273.

[6] K. Hercog, S. Maisanaba, M. Filipič, M. Sollner-Dolenc, L. Kač, B. Žegura, Genotoxic activity of bisphenol A and its analogues bisphenol S, bisphenol F and bisphenol AF and their mixtures in human hepatocellular carcinoma (HepG2) cells, Sci. Total Environ. 687 (2019) 267–276.

[7] A. Li, T. Zhuang, W. Shi, Y. Liang, C. Liao, M. Song, G. Jiang, Serum concentration of bisphenol analogues in pregnant women in China, Sci. Total Environ. 707 (2020), 136100.

[8] G. Xu, S. Ma, L. Tang, R. Sun, J. Xiang, B. Xu, Y. Bao, M. Wu, Occurrence, fate, and risk assessment of selected endocrine disrupting chemicals in wastewater treatment plants and receiving river of Shanghai, China, Environ. Sci. Pollut. Res. 23 (2016) 25442–25450.

[9] C. Huang, L.-H. Wu, G.-Q. Liu, L. Shi, Y. Guo, Occurrence and ecological risk assessment of eight endocrine-disrupting chemicals in urban river water and sediments of south China, Arch. Environ. Contam. Toxicol. 75 (2018) 224–235.

[10] M. Pirsaheb, H. Hossini, F. Asadi, H. Janjani, A systematic review on organochlorine and organophosphorus pesticides content in water resources, Toxin Rev. 36 (2017) 210–221.

[11] M.B. Ahmed, J.L. Zhou, H.H. Ngo, W. Guo, N.S. Thomaidis, J. Xu, Progress in the biological and chemical treatment technologies for emerging contaminant removal from wastewater: A critical review, J. Hazard. Mater. 323 (2017) 274–298.

[12] Y.-J. Lai, D.-J. Lee, Pollutant degradation with mediator Z-scheme heterojunction photocatalyst in water: A review, Chemosphere 282 (2021) 131059.

[13] L. Zhang, Y. Li, Q. Li, J. Fan, S.A.C. Carabineiro, K. Lv, Recent advances on bismuth-based photocatalysts: Strategies and mechanisms, Chem. Eng. J. 419 (2021), 129484.

[14] M. Xu, J. Yang, C. Sun, L. Liu, Y. Cui, B. Liang, Performance enhancement strategies of bi-based photocatalysts: A review on recent progress, Chem. Eng. J. 389 (2020), 124402.

[15] M. Hao, T. Yi, Y. Cao, Y. Song, Z. Cao, W. He, Y. Gao, J. Liu, Enhanced visible light photocatalytic activity in AgI/BiOCOOH composite, Adv. Powder Technol. 30 (2019) 111–119.

[16] J. Xiong, G. Cheng, Z. Lu, J. Tang, X. Yu, R. Chen, BiOCOOH hierarchical nanostructures: Shape-controlled solvothermal synthesis and photocatalytic degradation performances, CrystEngComm 13 (2011) 2381–2390.

[17] S. Li, J. Chen, Y. Liu, K. Xu, J. Liu, In situ anion exchange strategy to construct flower-like BiOCl/BiOCOOH p-n heterojunctions for efficiently photocatalytic removal of aqueous toxic pollutants under solar irradiation, J. Alloy. Compd. 781 (2019) 582–588.

[18] Q. Wang, G. Lv, Y. Cao, Z. Chen, J. Jia, Y. Qin, Z. Lin, X. Xie, Z. Wang, Rational design of 2D ultrathin $BiO(HCOO)_xI_{1-x}$ composite nanosheets: The synergistic effect of ultrathin structure and hybridization in the effective elimination of BPA under visible light irradiation, Sep. Purif. Technol. 282 (2022), 120153.

[19] X. Wang, X. Wang, J. Huang, S. Li, A. Meng, Z. Li, Interfacial chemical bond and internal electric field modulated Z-scheme S-v-$ZnIn_2S_4$/$MoSe_2$ photocatalyst for efficient hydrogen evolution, Nat. Commun. 12 (2021) 4412.

[20] F. Chen, Q. Yang, F. Yao, S. Wang, J. Sun, H. An, K. Yi, Y. Wang, Y. Zhou, L. Wang, X. Li, D. Wang, G. Zeng, Visible-light photocatalytic degradation of multiple antibiotics by AgI nanoparticle-sensitized $Bi_5O_7I$ microspheres: Enhanced interfacial charge transfer based on Z-scheme heterojunctions, J. Catal. 352 (2017) 160–170.

[21] C. Liu, Z. Han, Y. Feng, H. Dai, Y. Zhao, N. Han, Q. Zhang, Z. Zou, Ultrathin Z-scheme 2D/2D N-doped $HTiNbO_5$ nanosheets/g-$C_3N_4$ porous composites for efficient photocatalytic degradation and $H_2$ generation under visible light, J. Colloid Interface Sci. 583 (2021) 58–70.

[22] Y. Liu, J. Xu, M. Chen, Synthesis of direct Z-Scheme $Bi_3NbO_7$/BiOCl photocatalysts with enhanced activity for CIP degradation and Cr(VI) reduction under visible light irradiation, Sep. Purif. Technol. 276 (2021) 119255.

[23] Z. Guan, X. Li, Y. Wu, Z. Chen, X. Huang, D. Wang, Q.i. Yang, J. Liu, S. Tian, X. Chen, H. Zhao, AgBr nanoparticles decorated 2D/2D GO/$Bi_2WO_6$ photocatalyst with enhanced photocatalytic performance for the removal of tetracycline hydrochloride, Chem. Eng. J. 410 (2021) 128283.

[24] M. Chen, C. Guo, S. Hou, J. Lv, Y. Zhang, H. Zhang, J. Xu, A novel Z-scheme AgBr/P-g-$C_3N_4$ heterojunction photocatalyst: Excellent photocatalytic performance and photocatalytic mechanism for ephedrine degradation, Appl. Catal. B 266 (2020) 118614.

[25] L. Sun, W. Wu, Q. Tian, M. Lei, J. Liu, X. Xiao, X. Zheng, F. Ren, C. Jiang, In situ oxidation and self-assembly synthesis of dumbbell-like alpha-$Fe_2O_3$/Ag/AgX (X = Cl, Br, I) heterostructures with enhanced photocatalytic properties, ACS Sustainable Chem. Eng. 4 (2016) 1521–1530.

[26] Z. Hu, X. Xie, S. Li, M. Song, G. Liang, J. Zhao, Z. Wang, Rational construct CQDs/BiOCOOH/uCN photocatalyst with excellent photocatalytic performance for degradation of sulfathiazole, Chem. Eng. J. 404 (2021), 126541.

[27] Q. Li, J. Hu, H. Wang, Z. Wu, In situ synthesis of an advanced Z-scheme Bi/BiOI/black $TiO_2$ heterojunction photocatalysts for efficient visible-light-driven NO purification, Appl. Surf. Sci. 562 (2021), 150250.

[28] Q. Wang, Z. Liu, D. Liu, G. Liu, M. Yang, F. Cui, W. Wang, Ultrathin two-dimensional $BiOBr_xI_{1-x}$ solid solution with rich oxygen vacancies for enhanced visible-light-driven photoactivity in environmental remediation, Appl. Catal. B 236 (2018) 222–232.

[29] Y. Cui, X. Zhang, H. Zhang, Q. Cheng, X. Cheng, Construction of BiOCOOH/g-$C_3N_4$ composite photocatalyst and its enhanced visible light photocatalytic degradation of amido black 10B, Sep. Purif. Technol. 210 (2019) 125–134.

[30] D. Huang, J. Li, G. Zeng, W. Xue, S. Chen, Z. Li, R. Deng, Y. Yang, M. Cheng, Facile construction of hierarchical flower-like Z-scheme AgBr/$Bi_2WO_6$ photocatalysts for effective removal of tetracycline: Degradation pathways and mechanism, Chem. Eng. J. 375 (2019), 121991.

[31] N. Chang, Y.-R. Chen, F. Xie, Y.-P. Liu, H.-T. Wang, A promising Z-scheme heterojunction via loading Ag/AgCl into porous $Co_3O_4$ derived from ZIF-67 for visible light driven photocatalysis, Microporous Mesoporous Mater. 307 (2020), 110530.

[32] G. Fan, J. Zhan, J. Luo, J. Lin, F. Qu, B. Du, Y. You, Z. Yan, Fabrication of heterostructured Ag/AgCl@g-$C_3N_4$@UIO-66($NH_2$) nanocomposite for efficient photocatalytic inactivation of microcystis aeruginosa under visible light, J. Hazard. Mater. 404 (2021), 124062.

[33] H. Yu, D. Wang, B. Zhao, Y. Lu, X. Wang, S. Zhu, W. Qin, M. Huo, Enhanced photocatalytic degradation of tetracycline under visible light by using a ternary photocatalyst of $Ag_3PO_4$/AgBr/g-$C_3N_4$ with dual Z-scheme heterojunction, Sep. Purif. Technol. 237 (2020), 116365.

[34] Z. Zhang, Z. Pan, Y. Guo, P.K. Wong, X. Zhou, R. Bai, In-situ growth of all-solid Z-scheme heterojunction photocatalyst of $Bi_7O_9I_3$/g-$C_3N_4$ and high efficient degradation of antibiotic under visible light, Appl. Catal. B 261 (2020), 118212.

[35] Z. Wang, L. Jiang, K. Wang, Y. Li, G. Zhang, Novel AgI/$BiSbO_4$ heterojunction for efficient photocatalytic degradation of organic pollutants under visible light: Interfacial electron transfer pathway, DFT calculation and degradation mechanism study, J. Hazard. Mater. 410 (2021), 124948.

[36] C. Liang, H.-P. Feng, H.-Y. Niu, C.-G. Niu, J.-S. Li, D.-W. Huang, L. Zhang, H. Guo, N. Tang, H.-Y. Liu, A dual transfer strategy for boosting reactive oxygen species generation in ultrathin Z-scheme heterojunction driven by electronic field, Chem. Eng. J. 384 (2020), 123236.

[37] P. Chen, Q. Zhang, Y. Su, L. Shen, F. Wang, H. Liu, Y. Liu, Z. Cai, W. Lv, G. Liu, Accelerated photocatalytic degradation of diclofenac by a novel CQDs/BiOCOOH hybrid material under visible-light irradiation: Dechloridation, detoxicity, and a new superoxide radical model study, Chem. Eng. J. 332 (2018) 737–748.

[38] Y. Chen, X. Ji, S. Vadivel, B. Saravanakumar, Low-cost fabrication of BiOCOOH microflowers for high-performance supercapacitors applications, J. Mater. Sci.-Mater. Electron. 30 (2019) 8903–8910.

[39] W. Li, L. Jin, F. Gao, H. Wan, Y. Pu, X. Wei, C. Chen, W. Zou, C. Zhu, L. Dong, Advantageous roles of phosphate decorated octahedral $CeO_2$ {111}/g-$C_3N_4$ in boosting photocatalytic $CO_2$ reduction: Charge transfer bridge and lewis basic site, Appl. Catal. B 294 (2021), 120257.

[40] Y. Zhou, M. Yu, H. Liang, J. Chen, L. Xu, J. Niu, Novel dual-effective Z-scheme heterojunction with g-$C_3N_4$, $Ti_3C_2$ MXene and black phosphorus for improving visible light-induced degradation of ciprofloxacin, Appl. Catal. B 291 (2021), 120105.

[41] X.-J. Wen, C.-G. Niu, H. Guo, L. Zhang, C. Liang, G.-M. Zeng, Photocatalytic degradation of levofloxacin by ternary $Ag_2CO_3$/$CeO_2$/AgBr photocatalyst under visible-light irradiation: Degradation pathways, mineralization ability, and an accelerated interfacial charge transfer process study, J. Catal. 358 (2018) 211–223.

[42] B. Zhou, X. Zhao, H. Liu, J. Qu, C.P. Huang, Visible-light sensitive cobalt-doped $BiVO_4$ (Co-$BiVO_4$) photocatalytic composites for the degradation of methylene blue dye in dilute aqueous solutions, Appl. Catal. B 99 (2010) 214–221.

[43] T.A. Kurniawan, Z. Mengting, D. Fu, S.K. Yeap, M.H.D. Othman, R. Avtar, T. Ouyang, Functionalizing $TiO_2$ with graphene oxide for enhancing photocatalytic degradation of methylene blue (MB) in contaminated wastewater, J. Environ. Manage. 270 (2020), 110871.

[44] M.N.H. Rozaini, N. Yahaya, B. Saad, S. Kamaruzaman, N.S.M. Hanapi, Rapid ultrasound assisted emulsification micro-solid phase extraction based on molecularly imprinted polymer for HPLC-DAD determination of bisphenol A in aqueous matrices, Talanta 171 (2017) 242–249.

[45] J. Lv, X. Liu, P. Li, W. Jin, J. Xu, Y. Zhao, AgI loading BiOI composites with enhanced photodegradation efficiency for bisphenol A under simulated solar light, Sci. Total Environ. 669 (2019) 194–204.

[46] K. Zhu, Y. Sun, W. Jiang, C. Zhang, Y. Dai, Z. Liu, T. Wang, X. Guo, H. Jia, Inorganic anions influenced the photoaging kinetics and mechanism of polystyrene microplastic under the simulated sunlight: Role of reactive radical species, Water Res. 216 (2022), 118294.

[47] W. Hu, W. Tong, Y. Li, Y. Xie, Y. Chen, Z. Wen, S. Feng, X. Wang, P. Li, Y. Wang, Y. Zhang, Hydrothermal route-enabled synthesis of sludge-derived carbon with oxygen functional groups for bisphenol A degradation through activation of peroxymonosulfate, J. Hazard. Mater. 388 (2020), 121801.

[48] J. Xiao, Y. Xie, Q. Han, H. Cao, Y. Wang, F. Nawaz, F. Duan, Superoxide radical-mediated photocatalytic oxidation of phenolic compounds over $Ag^+$/$TiO_2$: Influence of electron donating and withdrawing substituents, J. Hazard. Mater. 304 (2016) 126–133.

[49] Y. Rao, Y. Zhang, J. Fan, G. Wei, D. Wang, F. Han, Y. Huang, J.-P. Croué, Enhanced peroxymonosulfate activation by Cu-doped $LaFeO_3$ with rich oxygen vacancies: Compound-specific mechanisms, Chem. Eng. J. 435 (2022), 134882.

[50] P. Hu, H. Su, Z. Chen, C. Yu, Q. Li, B. Zhou, P. Alvarez, M. Long, Selective degradation of organic pollutants using an efficient metal-Free catalyst derived from carbonized polypyrrole via peroxymonosulfate activation, Environ. Sci. Technol. 51 (2017) 11288–11296.

[51] Q. Wang, J. Lu, Y. Jiang, S. Yang, Y. Yang, Z. Wang, FeCo bimetallic metal organic framework nanosheets as peroxymonosulfate activator for selective oxidation of organic pollutants, Chem. Eng. J. 443 (2022), 136483.

[52] Q. Wang, Z. Xu, Y. Cao, Y. Chen, X. Du, Y. Yang, Z. Wang, Two-dimensional ultrathin perforated $Co_3O_4$ nanosheets enhanced PMS-Activated selective oxidation of organic micropollutants in environmental remediation, Chem. Eng. J. 427 (2022), 131953.
[53] M. Liu, J. Liu, K. Zhou, J. Chen, Q. Sun, Z. Bao, Q. Yang, Y. Yang, Q. Ren, Z. Zhang, Turn-on photocatalysis: creating lone-pair donor-acceptor bonds in organic photosensitizer to enhance intersystem crossing, Adv. Sci. 8 (2021) 2100631.
[54] K. Wang, Y. Li, G. Zhang, J. Li, X. Wu, 0D Bi nanodots/2D $Bi_3NbO_7$ nanosheets heterojunctions for efficient visible light photocatalytic degradation of antibiotics: Enhanced molecular oxygen activation and mechanism insight, Appl. Catal. B 240 (2019) 39–49.
[55] R. Cao, H. Yang, S. Zhang, X. Xu, Engineering of Z-scheme 2D/3D architectures with $Ni(OH)_2$ on 3D porous g-$C_3N_4$ for efficiently photocatalytic $H_2$ evolution, Appl. Catal. B 258 (2019), 117997.
[56] Y. Li, C. Gao, W. Jiang, C. Zhuang, W. Tan, W. Li, Y. Li, L. Wang, X. Liao, Z. Sun, J. Zou, X. Han, A game-changing design of low-cost, large-size porous cocatalysts decorated by ultra-small photocatalysts for highly efficient hydrogen evolution, Appl. Catal. B 286 (2021), 119923.
[57] Y. Guo, Q. Zhou, J. Nan, W. Shi, F. Cui, Y. Zhu, Perylenetetracarboxylic acid nanosheets with internal electric fields and anisotropic charge migration for photocatalytic hydrogen evolution, Nat. Commun. 13 (2022) 2067.
[58] J. Sun, Y. Hou, Z. Yu, L. Tu, Y. Yan, S. Qin, S. Chen, D. Lan, H. Zhu, S. Wang, Visible-light-driven Z-scheme $Zn_3In_2S_6$/AgBr photocatalyst for boosting simultaneous Cr (VI) reduction and metronidazole oxidation: Kinetics, degradation pathways and mechanism, J. Hazard. Mater. 419 (2021), 126543.
[59] X. Zhang, B. Lin, X. Li, X. Wang, K. Huang, Z. Chen, MOF-derived magnetically recoverable Z-scheme $ZnFe_2O_4/Fe_2O_3$ perforated nanotube for efficient photocatalytic ciprofloxacin removal, Chem. Eng. J. 430 (2022), 132728.
[60] Q. Liang, S. Ploychompoo, J. Chen, T. Zhou, H. Luo, Simultaneous Cr(VI) reduction and bisphenol A degradation by a 3D Z-scheme $Bi_2S_3$-$BiVO_4$ graphene aerogel under visible light, Chem. Eng. J. 384 (2020), 123256.
[61] B. Kim, J. Jang, D.S. Lee, Enhanced photocatalytic degradation of bisphenol A by magnetically separable bismuth oxyiodide magnetite nanocomposites under solar light irradiation, Chemosphere 289 (2022), 133040.
[62] L. Jing, D. Wang, M. He, Y. Xu, M. Xie, Y. Song, H. Xu, H. Li, An efficient broad spectrum-driven carbon and oxygen co-doped g-$C_3N_4$ for the photodegradation of endocrine disrupting: Mechanism, degradation pathway, DFT calculation and toluene selective oxidation, J. Hazard. Mater. 401 (2021), 123309.
[63] Q. Wang, Y. Cao, Y. Yu, C. Zhang, J. Huang, G. Liu, X. Zhang, Z. Wang, H. Ozgun, M.E. Ersahin, W. Wang, Enhanced visible-light driven photocatalytic degradation of bisphenol A by tuning electronic structure of Bi/BiOBr, Chemosphere (2022) 136276, https://doi.org/10.1016/j.chemosphere.2022.136276.